ISSN: 2366-1313

Proton radiography research employing machine learning techniques

Adivishnu N, Research Scholar, Department of Physics , Radha Govind University, Ramgarh,Jharkhand.

Dr. Sachin Saxena ,Assistant Professor ,Supervisor, Department of Physics ,Radha Govind University, Ramgarh, Jharkhand

Abstract : Newline One of the contemporary cancer treatment options with rising demand worldwide is proton therapy. However, the issue of range uncertainty, which lowers the standard of proton therapies, has yet to be addressed. The range uncertainty that results from the calibration curve that translates x-ray Hounsfield newline units (HU) to relative stopping power (RSP) called newline newline in this context, and proton imaging newline is a potential way for lowering newline uncertainty. A more modern method of proton newline imaging called proton energy resolved newline dose imaging (pERDI) is based on the energy dependency of the dose newline distribution produced by a scanned proton beam. The primary benefit of this method is the reduction in complexity of the setup due to the use of a single detector to measure the exit dosage with various beam intensities. newline This study uses the pERDI technology to present fresh ideas in the cutting-edge area of proton radiography. This thesis focuses on the pERDI technique to produce proton radiographs using a variety of methods, including the and#967;2-minimization technique, an analytical expression, and various machine learning (ML) methods, including neural networks from the Keras library, the Extreme Gradient Boosting (XGboost) algorithm, and advanced deep learning (DL) methods. newline The research on the newline accuracy that may be attained utilising the pERDI approach in homogeneous and heterogeneous newline media are presented in the first section of the thesis. The findings are encouraging since the feasible WEPL newline accuracy in a homogenous medium was within 1 mm utilising the Lynx detector, and all homogeneous inserts of tissue surrogates were measured with an RSP with a precision newline greater than 1.5%. newline The first findings showed that the newline vi newline pERDI approach can estimate the WEPL and RSP newline with clinically acceptable accuracy.

Keywords: Proton, Proton Therapies, Machine Learning.

ISSN: 2366-1313

I Introduction:

Although research on proton imaging in proton therapy was initiated about 60 years ago, the practical application has not yet been achieved. The range of protons is now determined from the xCT scans in all proton facilities. The electron densities of various tissue materials that are kept in HU are shown by xCT pictures. A calibration curve is used to quantify the protons' RSP from HU for therapy. This translation from HU to RSP puts uncertainty into the RSP calculation, which further translates into error in the proton range. Proton radiography and proton computed tomography are the two different forms of proton imaging. Protons are used to create two-dimensional (2D) pictures in pRG and three-dimensional (3D) images in pCT. In the beginning, in the 1960s and 1970s, there was a lot of research and interest in pRG and pCT. Later, xCT photos surpassed pRG and pCT images in popularity because to their higher resolution images. As a result, there was a fall in interest in proton imaging, and few experiments and studies were conducted for a while. Proton imaging methods have gained popularity in the last 20 years, and there has been a rise in interest in this area of research as a result of the expansion of proton treatment facilities across the globe. The range of the protons in the observed object is shown by pRG pictures, which may be directly extracted from photon-based images. The proton image has unique limits as well as additional advantages. The primary drawback is the poor picture quality in comparison to results from xCT procedures.

In contrast to photons, protons do not move through a medium in a straight path. From the nuclei's Coulomb field, protons are deflected. Multiple Coulomb Scattering, or MCS, refers to these many, random small-angle deflections of protons from atomic nuclei. Due to MCS, the protons travel further than the material's true thickness, resulting in poor spatial resolution in the reconstructed radiographs. The excitation and ionisation of the atomic electrons cause the charged particles in our research, protons, to lose energy. According to the Bethe-Bloch formula (1), the speed of the particles in the medium being traversed has an inverse relationship with the rate of energy loss. All the protons with a certain energy should come to an end at a certain depth

ISSN: 2366-1313

(range of protons) in the material. Any proton in the medium will halt at a different depth depending on statistics [2]. With a standard deviation in range straggling surpassing 1%, fluctuations in the proton range (referred to as range straggling) are linked to variations in the energy straggling [3].

Proton Imaging

Proton radiography and proton computed tomography were introduced in 1963 by Cormack . These techniques might be developed and have some benefits over traditional X-ray computer tomography. The limited spatial resolution of pCT was found to be a major obstacle for the creation of images. The multiple scattering event is the result of the small angle deflections that occur in the protons' trajectory due to interactions between the Coulomb fields on the nucleus and the absorbent material.

Proton imaging has yet to be incorporated into the clinical routine. Many academic studies are underway to improve access to proton therapy once significant technical obstacles have been overcome.

II Litreature Survey

The physics of proton therapy is discussed in this chapter, along with the interactions of various particles in water, the link between proton energy and range, the many treatment modalities used in proton therapy, as well as its benefits and drawbacks. Radiation therapy's primary objective in the treatment of cancer is to deliver as much energy as possible to the tumour in order to damage its DNA and halt the proliferation of uncontrolled cells while protecting nearby healthy tissues and the OAR from needless radiation. Proton therapy, as the name implies, employs protons to treat tumours instead of the high-energy photons and electrons that are employed in conventional radiation treatment to treat cancer.

Particles may disperse, leave energy behind, or even halt as they go through matter. The kind of particle, energy, beam intensity, and density of the substance it goes through all affect the amount of energy deposited per unit mass, or dosage. The cancer should get the highest dosage possible while the surrounding tissues only receive the bare minimum. Numerous research are now being conducted to help

ISSN: 2366-1313

accomplish this and enhance the quality of life after therapy. [4–6].

The depth-dose distribution provides the dosage deposited by various particles moving through a material medium. The distribution of depth-dose for charged and neutral particles in water [7].

These particles' depth-dose profiles exhibit a brief area of dose build-up followed by an exponential decrease. These particles cause the atomic electrons to move by interacting with the surrounding material, transferring energy to them, and doing so. Since the radiation is delivered by these secondary electrons directly to the tumour, their initial number rapidly declines. Even after passing through the water tank, the particles that do not interact with the medium will stay the same as when they first enter.

These particles exhibit a flat-dose plateau, a "Bragg peak"—a strong peak—and an area of dose fall-off. Compared to other heavy ions, protons have a dosage that is negligible or nonexistent beyond the Bragg peak. As the mass of the ions grows, the Bragg peak gets sharper, and at the same time, the ions exhibit a residual dose that results from nuclear fragmentation after the Bragg peak. To protect the healthy tissues, protons are favoured over other particles while treating tumours.

On the other hand, when considered as a radiological technique for age estimate, magnetic resonance imaging is unquestionably non-invasive and radiation-free. However, it may not be particularly successful in finding ossification centres and is highly extensive, costly, has logistical issues, and calls for a more precise methodology [8].

However, ultrasonography may be seen as a radiation-free, reliable, quick, economical, and nonionizing imaging process when compared to the aforementioned radiological modalities for age determination. However, there are currently only a small number of research on the use of skeletal ultrasonography in forensic age diagnosis [9]. Tanner JM et al. discovered in another study that there is significant intra- and inter-individual variation in the interpretation of radiographs, and they made attempts to increase reliability by creating pattern

ISSN: 2366-1313

recognition software that would enable computer-assisted radiographic bone age determination [10-11].

The TW approach is more accurate than the GP method since it is based on a more reliable mathematical foundation, but it is also more time-consuming and harder to implement, according to Alessandro et al. who compared the traditional and recently devised methods for skeletal age assessment [12].

But we cannot overlook the reality that small children, women who are childbearing age, and sometimes pregnant women make up the very demographic arriving for age assessment, where radiation exposure, no matter how slight, presents a serious threat to health [14]. Radiations in the form of exposure with radiological techniques that employ one kind of X-ray beam or another may result in a variety of negative consequences, such as dermatitis, infertility, cancer, etc. Therefore, even a little danger of radiation exposure should be of concern, particularly in the current environment, where it is crucial to follow ethical guidelines for any activity involving research on human beings. Additionally, there are some areas, like the clavicle, where radiographs in adults result in radiation doses similar to those from A CT scan of a clavicle is significantly more accurate than other methods, including an orthopantomogram (0.02 mSv), and a radiograph taken on the hand (0.0001mSv). [13–14].

III Methodology

Each proton's leftover energy or residual range, as well as its placements before and after the target, are monitored using proton tracking devices. A calibration between the signal in a detector and the route length travelled with averaged across several protons is achieved in proton integrating systems. WePL readings from the 2-D pRG pictures may be utilised to confirm treatment plans and provide information on the protons' range. There are three-dimensional volumetric WEPL values in the data from pCT. Using these WEPL values, the RSP of protons is calculated throughout the picture reconstruction process.

ISSN: 2366-1313

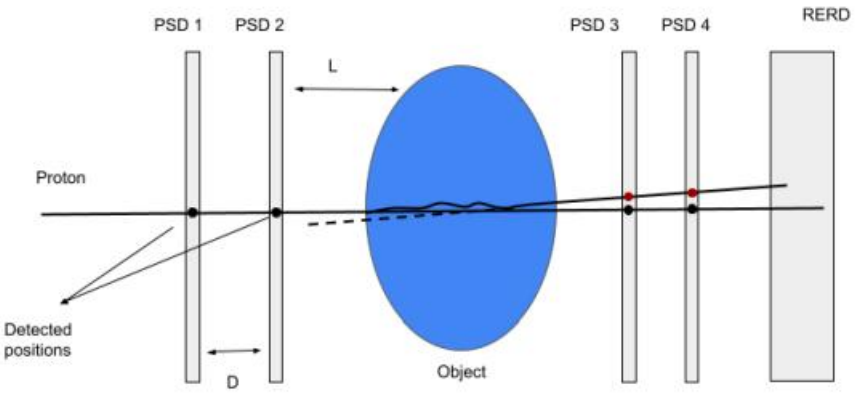

Figure 1 : Proton tracking system with position sensitive detectors (PSDs) and residual energy-range detector (RERD) schematically shown in . Drawing modified from [13].

Koehler reported the first pRG results in 2019 [15], then in 2020 [16] the findings of the pCT inquiry. Koehler displayed the poor spatial resolution and high contrast proton radiograph of an aluminium absorber. As a result of scattering, the experiment's proton beam's energy dropped from 160 MeV to 137 MeV, stopping

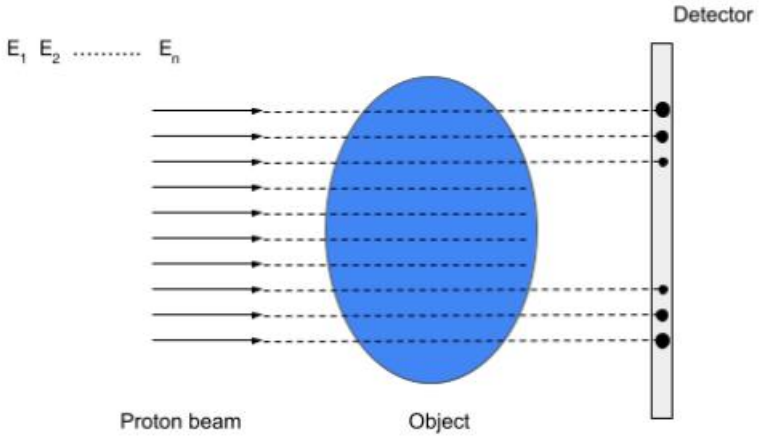

Figure 2 shows the proton integrating system schematically.

where the photographic film was positioned. He established a relationship between proton flux and depth, and the steepness of the flux-depth curve allowed for the thickness of the imaged object to be determined [17].

A transport system and gantry with moveable components are part of the experimental setup at PSI, which can

ISSN: 2366-1313

provide energy up to 270 MeV. Figure 3 displays the experimental setup's schematic depiction.

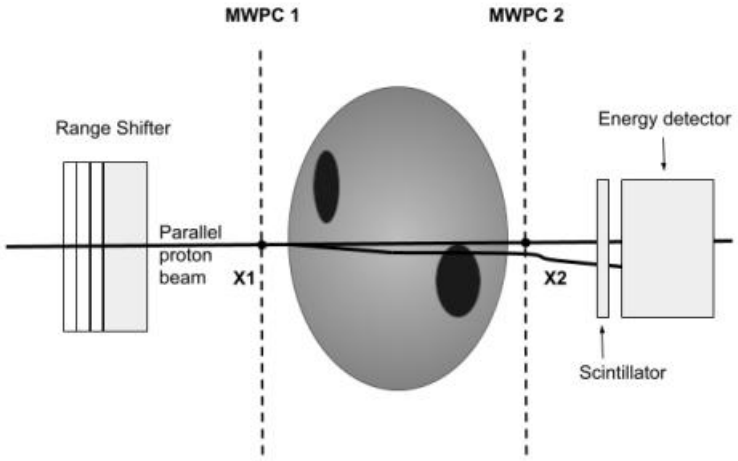

Figure 3.3: Schematic illustration of the PSI's experimental setup. Image used with permission.

Two position-sensitive multiwire proportional chambers (MWPC) are used in the experiment and are positioned before and after the test item. The 590 MeV proton was downgraded to 219 MeV by passing the proton beam via a range changer. After passing through the test item and being identified by MWPC2, the protons were first detected in MWPC1. The beam continues on to the scintillator before coming to a halt at the NaI energy detector. Reconstructing the intercepts of each event's most probable route between MWPC1 and MWPC2 was done as part of the study [16].

IV Experiments and Results

Resource and Techniques

The range-shift maps derived from simulations of PR in 40 patients with head and neck disorders have been analysed using CNNs. Each PR field had a varied size and was located in a distinct part of the body. The shift maps that came from each sort of PR field were categorised by a CNN expert.

The PR Simulations

To simulate PRs, OpenREGGUI was utilised as an open-source Matlab toolbox [8],[12]. The Giraffe MLIC

ISSN: 2366-1313

(Multi-Layer Ionisation Chamber) PRs (IBA Dosimetry Schwarzenbruck DE) may be simulated with this technique. This technology can model the creation of PR.

An air MLIC is used as input in the simulations. The patient's water equivalent thickness (WET), as estimated by the CT imaging, is then used to scale integral depth dose (IDD) curves along the beam axis. The technique uses a Gaussian kernel to combine the air IDDs with the beam sigma of 3.5mm to account for range-mixing. As the IDD reference is an actual MLIC measurement these simulations are close to true measurement noise. The PR simulations used 210 MeV pencil beams with a 270-degree gantry and 1mm spacing between pencil beams. The research was based on planning CT images of 40 head and neck cancers patients that had received previous treatment at our facility.

To evaluate the efficacy of this strategy in various anatomical placements and with varying PR field widths, PR fields are simulated. It was decided to cover the patient's head and neck with a 26 x 26 cm2 PR field. At the base of the head and neck, two minuscule areas, each measuring 4.5 by 4.5 cm2, were likewise reconstructed. Fields A, B, and C are the names of the three fields. Their location is shown in Figure 1 together with a patient geometry example. Field A's size was chosen to include the head and neck. To make the most of the readout space on the MLIC, the sizes of fields B and C have been selected. This was done in accordance with previous investigations using an MLIC. Three fields were chosen to cover different tissues along the beam. The presence of heterogeneity on the lateral side was also encouraged, as it produces different Bragg curves which help to identify setup mistakes [9].

Mistaken situations

For each patient's CT image, a reference PR was created to imitate an unaltered range measurement. Reference radiographs were contrasted with radiographs in which the proton range was altered by one or more causes of inaccuracy. Setup errors and errors in the calibration curve were considered as sources of error. The Table 1 shows the values for density and the Hounsfield Unit (HU) of the general calibration curve, which

ISSN: 2366-1313

represents a reference condition that has not been altered. By altering the density values in the calibration curves for the soft (S) and hard (B), tissue sections, calibration curve errors may be reproduced.

CNNs corresponding to fields A, B, and C were given variable sizes and different numbers of convolutional layers. For instance, the CNN allocated to field A has four convolutional layers with two having 32 and two having 64 filters, each with a size of three. A max pooling layer, which follows each convolutional layer, minimises the size of the representation by extracting the maximum value from each convolution. An activation function for the rectifier linear unit (ReLu) then reduces all negative inputs to zero. Two layers are linked together by adding the result of the layer pooling (for example, it is modified and flattened). In the first layer, an activation function named ReLu will be used.

CT scans from 30 patients served as the training, validation and testing datasets to create range-shift maps. Twenty PR simulations were run for each CT scan. Two of each category of mistake with different magnitudes was used. Simulations of error combinations involved forty patients. Each patient had 24 maps of range shift created, which corresponds with the possible mistake combinations shown in Table 2. Each CNN is trained using 1120 maps, 400 of which are from individual mistakes and 720 from combinations. Each error type is equally represented. The 10% map set was randomly chosen to be used as a training aid. The 10 remaining range shifts for patients were assigned to the

Test cases The CNNs were not previously introduced to any of the patients that had been used for the testing. Table 3 shows that one set of testing (known as test isolated, or TI), consisted of 200 range-shift maps for one type mistake. Another set contained 240 range-shift maps.

Measurement metrics

For each range shift map in the testing sets, a prediction vector was created when the training procedure was complete. Based on a threshold of 0.5, each prediction v ctor value was divided into two groups. Predictions were labelled as positive or negative for that mistake based on whether they were above or below the threshold.

ISSN: 2366-1313

The resultant binary prediction vectors are therefore prepared for comparison with their corresponding actual values (label) once the threshold has been applied. The exact, incorrect, and partial match percentages were used to evaluate the accuracy of the forecasts. The term "exact matching" is used when every element of a binaryized prediction vector exactly matches the corresponding real values. It is regarded as an invalid match when none of the recognised fault kinds in a map range shift are present. Partial matches happen when certain components of the prediction vector match the label but the prediction vector and binarized value vector are not the same. If a range-shift map includes just one kind of mistake and the CNNs anticipate two types of errors, partial matches may also happen in TI.

The percentages of precise matches, partial matches, and wrong matches for CNNs allocated to A, B, and C were computed in T and TC. Five categories make up the TI assessment: S, B, F, AP, and IS. For the six mistake combination sets S and IS, B and AP, B and IS, F and AP and IS, we estimated the exact, erroneous, and partial match for TC.

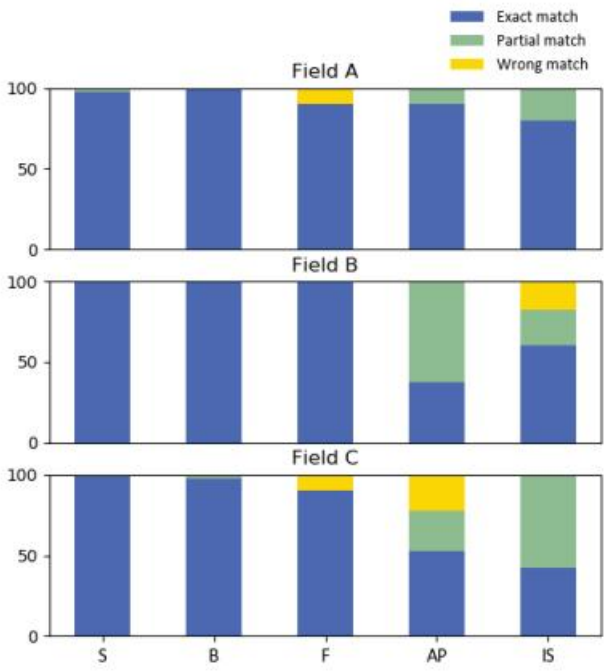

Figure 4 Percentages of exact, partial, and incorrect matches for each class type the other categories follow suit.

ISSN: 2366-1313

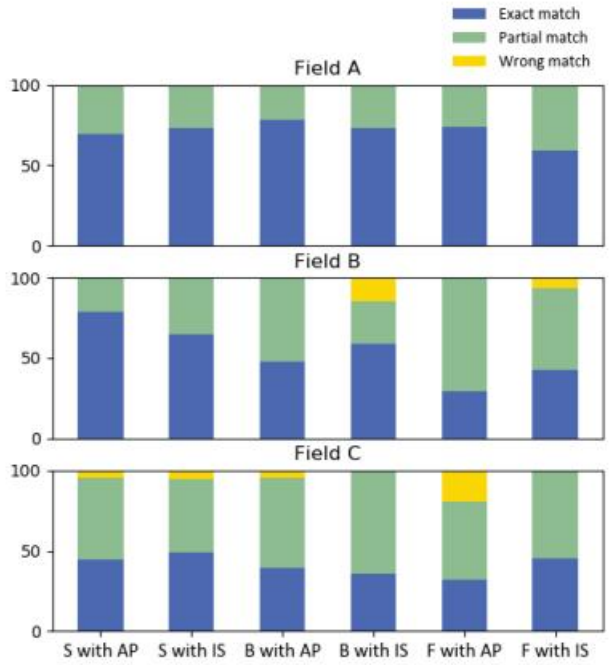

Figure 5 : Calculated percentages of exact, incomplete, and incorrect matches for various groupings .

CNNs do better than TI or TC when they classify range shifts maps with isolated mistakes, rather than classifying combinations. In fields A, C, and B the percentages of exact matches are 92% for individual mistakes and 80% for combinations, correspondingly, 78%. In terms of exact matches, 71%, 54% and 41% are the percentages. In TI only a very small number of maps are partially classified, but this is not the case in TC

Figure 4 for TI reports a subsequent performance review broken down by error type. Exact match percentages for calibration curve mistakes are often quite close to 100%. A somewhat worse result is achieved for mistakes of type F, where 10% of fields included incorrect matches.

A and C. In comparison to calibration curve errors, setup error predictions have a greater incidence of partial matches. The most relevant instances may be found in field B's AP mistakes (62% of partial matches) and field C's IS faults (57% of partial matches). IS mistakes both had wrong match rates of 17% and 22%, respectively. The results of CNN's performance for various sorts of combinations (using TC) are shown in Figure 5. Since the exact match percentages for all sorts of

ISSN: 2366-1313

combinations vary from 59% to 78%, field A performs better than fields B and C. Field B exhibits significant performance variability for various combinations of error kinds. For instance, the exact/partial match ratio for the combination of S and AP is 79/21%, whereas the ratio for the combination of F and AP is 48/52%. The performance of the CNN in field C is consistent across several combinations, with exact match percentages ranging from 32% to 49%.

Three CNNs were able to identify instances where a calibration error and an incorrect setup was both found. In this case, field A produced the best results. Fields B andC followed. Position of PR fields also affects the CNN's ability to recognize combinations of errors. The field B at the top of the head yields a 13% greater exact match percentage than Field C when two fields are of similar size. In an ideal site, every mistake will result in a pattern that is distinct and easily recognisable. Moreover, all tissues that are to be used in the calibration should also be in the anatomical region.

These demands aren't usually entirely attainable. For instance, there are slight range changes because the head and neck area has less fat tissue than other tissues. In particular, when they occur in conjunction with setup errors (figure 2), range shifts caused by type F mistakes can cause problems for CNNs. Figure 2 shows that range shifts caused by faults of Type F can be as bad or worse than those produced by Errors of Type S. Figure 4 demonstrates how calibration curve mistakes may be quickly seen when they occur alone. Although there are more partial matches than complete matches, setup problems are often observed. In certain circumstances, CNN forecast both the preexisting setup fault and an additional sort of error. In most cases, calibration errors are more important than setup mistakes. CNNs have been trained to identify two types of errors in maps that are dominated by setup faults. The result is not a constraint, since the CNN can detect setup errors and realign the patient if necessary. To confirm there are no more calibration curves, a second PR may be acquired. Otherwise, local setup troubles would persist. The PR field has to be sized to a suitable compromise. Alternative methods for minimising setup mistakes,

ISSN: 2366-1313

such as those established by Deffet and colleagues [12], might be added to CNNs to aid in the identification of additional possible sources of error impacting the proton range.

V Conclusion

It was shown that using CNNs, it is possible to categorise PR photos that are distorted by various proton range errors. Patients with head and neck cancer underwent PR simulations that included both individual and combined setup and calibration curve flaws. The examined technique offers tools for automated PR interpretation in the quality assurance procedure for proton therapy.

VI References:

[1] H. Paganetti, "Range uncertainties in proton therapy and the role of Monte Carlo simulations," Physics in Medicine and Biology, vol. 57, no. 11, 2012, doi: 10.1088/0031-9155/57/11/R99.

[2] A. C. Knopf and A. Lomax, "In vivo proton range verification: A review," Physics in Medicine and Biology, vol. 58, no. 15, pp. 131–160, 2013, doi: 10.1088/0031-9155/58/15/R131.

[3] J. Unkelbach, T. C. Y. Chan, and T. Bortfeld, "Accounting for range uncertainties in the optimization of intensity modulated proton therapy," Physics in Medicine and Biology, vol. 52, no. 10, pp. 2755–2773, 2007, doi: 10.1088/0031-9155/52/10/009.

[4] K. Parodi and J. C. Polf, "In vivo range verification in particle therapy," Medical Physics, vol. 45, no. 11, pp. e1036–e1050, 2018, doi: 10.1002/mp.12960.

[5] A. Fredriksson, A. Forsgren, and B. Hårdemark, "Minimax optimization for handling range and setup uncertainties in proton therapy," Medical Physics, vol. 38, no. 3, pp.1672–1684, 2011, doi: 10.1118/1.3556559.

[6] M. Mumot, C. Algranati, M. Hartmann, J. M. Schippers, E. Hug, and A. J. Lomax,"Proton range verification using a range probe: Definition of concept and initial analysis," Physics in Medicine and Biology, vol. 55, no. 16, pp. 4771–4782, 2010, doi:10.1088/0031-9155/55/16/010.

[7] W. D. Newhauser and R. Zhang, "The physics of proton therapy," Physics in Medicine and Biology, vol. 60, no. 8, pp. R155–R209, 2015, doi: 10.1088/0031-9155/60/8/R155.

ISSN: 2366-1313

[8] P. Farace, R. Righetto, S. Deffet, A. Meijers, and F. vander Stappen, "Technical Note:A direct ray-tracing method to compute integral depth dose in pencil beam proton radiography with a multilayer ionization chamber," Medical Physics, vol. 43, no. 12,pp. 6405–6412, 2016, doi: 10.1118/1.4966703.

[9] P. Farace, R. Righetto, and A. Meijers, "Pencil beam proton radiography using a multilayer ionization chamber," Physics in Medicine and Biology, vol. 61, no. 11, pp.4078–4087, 2016, doi: 10.1088/0031-9155/61/11/4078.

[10] A. Hammi, S. Koenig, D. C. Weber, B. Poppe, and A. J. Lomax, "Patient positioning verification for proton therapy using proton radiography," Physics in Medicine andBiology, vol. 63, no. 24, 2018, doi: 10.1088/1361-6560/aadf79.

[11] A. Hammi, L. Placidi, D. C. Weber, and A. J. Lomax, "Positioning of head and neck patients for proton therapy using proton range probes: A proof of concept study," Physics in Medicine and Biology, vol. 63, no. 1, 2018, doi: 10.1088/1361-6560/aa9cff.

[12] S. Deffet, B. Macq, R. Righetto, F. vander Stappen, and P. Farace, "Registration ofpencil beam proton radiography data with X-ray CT," Medical Physics, vol. 44, no. 10, pp. 5393–5401, 2017, doi: 10.1002/mp.12497.

[13] U. Schneider, P. Pemler, J. Besserer, E. Pedroni, A. Lomax, and B. Kaser-Hotz, "Patient specific optimization of the relation between CT-Hounsfield units and proton stopping power with proton radiography," Medical Physics, vol. 32, no. 1, pp. 195–199, 2005, doi: 10.1118/1.1833041.

[14] U. Schneider and E. Pedroni, "Proton radiography as a tool for quality control in proton therapy," Medical Physics, vol. 22, no. 4, pp. 353–363, 1994, [Online]. Available: https://doi.org/10.1118/1.597470

[15] P. J. Doolan, M. Testa, G. Sharp, E. H. Bentefour, G. Royle, and H. M. Lu, "Patient-specific stopping power calibration for proton therapy planning based on single-detector proton radiography," Physics in Medicine and Biology, vol. 60, no. 5, pp.1901–1917, 2015, doi: 10.1088/0031-9155/60/5/1901.

[16] K. H. Cha, L. Hadjiiski, R. K. Samala, H. P. Chan, E. M. Caoili, and R. H. Cohan,"Urinary bladder segmentation in CT urography using deep-learning convolutional neural

ISSN: 2366-1313

network and level sets," Medical Physics, vol. 43, no. 4, pp. 1882–1886, 2016, doi: 10.1118/1.4944498.

[17] K. H. Jin, M. T. Mccann, E. Froustey, and M. Unser, "Deep Convolutional Neural Network for Inverse Problems in Imaging," in IEEE transactions on image processing, 2017, vol. 26, no. 9, pp. 4509–4522.

[18] A. Thummerer et al., "Comparison of CBCT based synthetic CT methods suitable for proton dose calculations in adaptive proton therapy," Physics in Medicine & Biology, 2020, doi: 10.1088/1361-6560/ab7d54.

[19] D. Nguyen et al., "A feasibility study for predicting optimal radiation therapy dose distributions of prostate cancer patients from patient anatomy using deep learning," Scientific Reports, vol. 9, no. 1, pp. 1–10, 2019, doi: 10.1038/s41598-018-37741-x.

[20] B. Sahiner et al., "Deep learning in medical imaging and radiation therapy," Medical Physics, vol. 46, no. 1, pp. e1–e36, 2019, doi: 10.1002/mp.13264.

[21] C. G. Ainsleya and C. M. Yeager, "Practical considerations in the calibration of CT scanners for proton therapy," Journal of Applied Clinical Medical Physics, vol. 15, no. 3, pp. 202–220, 2014, doi: 10.1120/jacmp.v15i3.4721.

[22] N. Peters et al., "Experimental assessment of inter-centre variation and accuracy in stopping power ratio prediction within the European Particle Therapy Network," 2019.